Available online at www.sciencedirect.com

ScienceDirect

Advances in Space Research xx (2021) xxx-xxx

ADVANCES IN SPACE RESEARCH
(a COSPAR publication)

www.elsevier.com/locate/asr

Ionospheric Disturbances in Mexican Territory Produced by Objects Entering the Atmosphere from Space

Jorge Tarango-Yong[a,*], Mario Rodriguez-Martinez[a,**], Raul Gutiérrez-Zalapa[a,1]

[a]*Escuela Nacional de Estudios Superiores, UNAM, campus Morelia, Antigua Carretera a Pátzcuaro No. 8701 Col. Ex Hacienda de San José de la Huerta, Morelia, Michoacán, 58190, México*

Received 1 May 2013; Received in final form 10 May 2013; Accepted 13 May 2013;
Available online 15 May 2013

Abstract

Please type your abstract here, and the rest of the text, figures, tables, equations etc. in the main body. Please do not modify LaTeX commands unless you need to modify them and know how to do it.

Keywords: Space Sciences; Atmosphere

1. Introduction

The Earth's magnetic field represents a final obstacle to the Solar Wind (SW) flux. When descelerated and defected by a non colisional shock wave in the flux direction, generates a cavity known as magnetosphere (Blanco-Cano et al., 2004). Since the Earth is embedded in this SW flux, is known that under adequated physical conditions (e.g magnetic reconnection) may exist some coupling between the magnetosphere and the Earth's ionosphere (Zolesi & Cander, 2014; Cnossen et al., 2012).

The Sun plays an important role in the physical proccesses that occur in the terrestrial magnetosphere-ionosphere system. When the SW interacts with the Earth's magnetosphere, particles may permeate the internal region via magnetic reconnection and penetrate to polar zones and generate boreal or austral auroras thus altering the system (Vázquez et al., 2016; Oka et al., 2011). By the other hand, the Extreme Ultraviolet Radiation (EUV) and X-rays coming from the Sun may interact with the neutral atmoshere via photoionization (Vlasov & Kelley, 2010). However, in both cases the final result is that the ionosphere's free electrons population is altered.

Some Ionospheric Perturbations (IP) become relevant due to their spatial and temporal scale in the Space Weather scenario. At intermediate latitudes, the most common in the ionosphere are known as Traveling Ionospheric Disturbances (TIDs). Typically they divide into two groups: a) large scale TIDs, associated with geomagnetic storms with sizes of $\sim$2000 km, periods of $\sim$1 h and velocities of $\sim$700 km s^{-1}, and b) Medium-scale TIDs, which are not fully associated with geomagnetic storms, present sizes of $\sim$100 km, periods from 10 minutes to 1 hour and velocities between 50 km s^{-1} and 1×10^2 km s^{-1} (Helmboldt et al., 2012). Diverse methods have benn used to study TIDs, such as incoherent dispersion radars, high frequency Doppler emmisors, data from Global Positioning System (GPS) stations or even radiotelescopes like the VLA or the Mexican Array Radio Telescope (MEXART) (Chilcote et al., 2015; Rodríguez-Martínez et al., 2014).

On the other side, the Earth's ionosphere may be affected or modified by other proccesses, particularly there are studies that show how the Vetical Total Electron Content (vTEC) due to shock waves generated for rockets launched to space (Lin et al., 2014). Similar proccesses modify the Earth's ionosphere due to objects entering the athmosphere from space, such as meteoroids like the one which fell on Chelyabinsk at 2013 (Yang et al., 2014). Previously, the ionospheric perturbations pro-

*Tel.: +52-443-476-5525;
email: jorge.tarango@comunidad.unam.mx
**email: m.rodriguez@enesmorelia.unam.mx

https://dx.doi.org/10.1016/j.jasr.xxxx.xx.xxx
0273-1177/

duced by this object were studied using two independent methods: a) detecting vTEC pertubations using GPS station near the impact location. And b) a wavelets analysis for detection of ...

In 2020 a meteoroid passed in mexican territory through mexican territory, which also was studied (Sergeeva et al., 2021). The meteoroid was recorded with outdoor cameras in different locations. The trajectory could be estimated, as well as other physical parameters.

In this work we will show a similar analysis for a sample of meteoroids detected in mexican territory by different methods. The first subsample consists in objects detected by the Geostationary Lightning Mapper (GLM) whose sizes are estimated between a few decimeters to meters in diameter (Goodman et al., 2013; Jenniskens et al., 2018; Rumpf et al., 2019). The second subsample will consist in objects detected by ocular witnesses from the American Meteor Society and as comparisson we will include the morelian meteoroid reported in Sergeeva et al. (2021) and the Chelyabinsk event Yang et al. (2014). The paper is arranged in the following way: §2 describes the samples of meteoroids as well of the properties that can be obtained from direct observations. Also describes the GPS data corresponding to the dates and locations where each object was located. §3 shows physical parameters of meteoroids obtained from the observed heights and energies. Finally, section §4 shows the vTEC maps and scintillation indices obtained from GPS observations.

2. Methodology

2.1. Meteors Databases

We selected a sample of meteors which were observed in mexican territory from the Geostationary Lightning Mapper (Goodman et al., 2013). Orignally this project was designed to detect ligthning activity in earth's athmosphere, but has been proven that also can detect bolides entering the athmosphere. The detection comes from two satellites called GOES-16 and GOES-17 orbiting the earth in geostationary orbits. We used the interactive database available at `https://neo-bolide.ndc.nasa.gov/#/`. These data are publicly available and easily downloaded from the same website. For each event we can obtain the recorded trajectory of meteors and the corresponding light curve. THe GLM satellites have an umbral magnitude for detection of -14. At this magnitude, a meteor is considered a bolide, and is expected to be at least decimeter-sized (in diameter) to reach such brightness. In the other hand, too bright meteors will saturate the detectors, and thus, lowering the quality of data. The result of this factors implies that the range in size of the objects in our sample varies in diameter between decimeter to meter size. Each event also has assigned a confidence ratio, from low confidence to high, depending in how bright is the event itself and if the trajectory recorded by GLM ressembles (or not) a straight line. We chose only events whose confidence ratio is high, in oreder to be sure we chose the brightest objects, and thus, in the diameter size of bolides, we favored the meter-sized ones. In table 1 we list the object we chose to do this work, order in chronological order. The columns of the table, from left to right are and ID to enumerate the meteors in the sample, the date and time each meteor was detected, the duration of the detection, their respective coordinates and the estimated height of the meteor over the ground at the time of the detection. GOES-16 and GOES-17 systematically detect the meteors at slightly different positions and at slightly different times, so we calculated the mean of the duration, latitude and longitude reported by both satellites for each event, and used the standard deviation as the uncertainties.

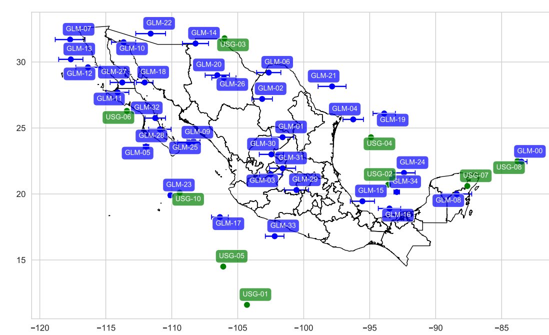

Fig. 1. Positions of events from table 1 (blue) and table 2. The events GLM-00/USG-08 actually correpond to the same bolide, but there are little discrepancies about the position where the bolide was detecte. The same applies for the events GLM-23/USG-10 and GLM-Ven/USG-09, which not appears in the map.

From table 1 is also clear that the duration of all the bolides detection last less than a second. This obsevation suggests that the bolides remain undetected by the GLM satellites until they get fragmented due to stagnation presure when they release a huge amount of energy and thus they become detectable.

By the other hand, we got another sample of 10 bolidesfrom US Goverment (USG) sensors from the Center for Near Earth Object Studies (CNEOS), publicly available at `https://cneos.jpl.nasa.gov/fireballs/`, where we may obtain directly data about bolides position, the date and time each bolide was detected, the energy released at fragmentation, the velocity and the height (the last two not availble for all bolides). As seen in table 2, the time span is quite larger, and the released energy is generally larger. Both energy distributions are compared directly in figure 2. Some elements appear in both samples, since are bright enough to be detected regardless the project involved. In USG sample, the total energy of each meteor is obtained directly, but is not the case for the GLM sample. In appendix Appendix A and Appendix B we give details about how this total energy is obtained.

2.2. GPS data

The Total Electron content along the integrated path of the link (s_i) at the frequency f_i can be inferred from the phase delay

Table 1. List of bolides detected in mexican territory (plus one detected near Venezuela and one detected near Cuba), detected by the Geostationary Lighning mapper. The events are listed in chronological order. The listed duration, latitude and longitude correspond to the mean of the measurements of both GOES satellites. The uncertainties correspond to the respecting mean deviation.

ID	Date of event	Start Time (UT)	Duration (seconds)	Latitude (deg)	Longitude (deg)	Altitude (km)	Energy (kT)
GLM-00	2019-02-01	18:17:09	2.651 ± 0.4907	22.45 ± 0.071	-83.50 ± 0.424	24	2.0978196 +/- 0.42361329
GLM-01	2019-05-23	16:36:18	0.197 ± 0.0000	24.30 ± 0.000	-101.60 ± 0.849	28	0.011954659 +/- 7.4054404e-3
GLM-02	2019-07-18	14:30:30	0.058 ± 0.0000	27.20 ± 0.000	-103.15 ± 0.778	72	5.7827709e-3 +/- 3.9334336e-3
GLM-03	2019-08-10	11:18:48	0.199 ± 0.0757	21.50 ± 0.000	-102.50 ± 0.849	92	0.010556123 +/- 6.6488245e-3
GLM-04	2019-10-03	07:55:33	0.106 ± 0.0297	25.65 ± 0.071	-96.25 ± 0.778	74	2.9915536e-3 +/- 2.2000998e-3
GLM-05	2019-10-09	06:08:11	0.103 ± 0.0078	23.60 ± 0.000	-111.95 ± 0.212	32	0.021837042 +/- 0.012429732
GLM-06	2019-11-16	09:36:04	0.396 ± 0.0134	20.30 ± 0.000	-100.55 ± 0.919	82	7.5423706e-3 +/- 4.9626060e-3
GLM-07	2019-11-17	15:36:01	0.116 ± 0.0035	31.70 ± 0.000	-117.70 ± 1.131	88	0.022397444 +/- 0.012701445
GLM-08	2019-11-19	07:57:40	0.097 ± 0.1138	20.00 ± 0.000	-88.40 ± 1.131	99	1.5012507e-3 +/- 1.1909667e-3
GLM-09	2019-11-26	13:23:20	0.078 ± 0.0290	23.90 ± 0.000	-108.70 ± 0.849	81	4.9551290e-3 +/- 3.4345742e-3
GLM-10	2019-12-04	09:42:54	0.173 ± 0.0028	31.50 ± 0.000	-113.65 ± 0.919	77	0.029149047 +/- 0.015891049
GLM-11	2019-12-15	14:50:49	0.127 ± 0.0134	27.70 ± 0.000	-114.10 ± 0.849	78	0.010556123 +/- 6.6488245e-3
GLM-12	2019-12-29	16:16:35	0.062 ± 0.0134	29.60 ± 0.000	-116.35 ± 0.919	79	4.2084911e-3 +/- 2.9746446e-3
GLM-13	2020-01-03	14:10:17	0.113 ± 0.0085	30.20 ± 0.000	-117.65 ± 0.919	74	0.011607116 +/- 7.2187549e-3
GLM-14	2020-01-06	16:39:27	0.118 ± 0.0042	31.40 ± 0.000	-108.20 ± 0.990	81	0.015448801 +/- 9.2392402e-3
GLM-15	2020-01-15	15:00:33	0.213 ± 0.1351	19.45 ± 0.071	-95.55 ± 0.919	93	0.012559739 +/- 7.7284725e-3
GLM-16	2020-02-12	09:25:40	0.210 ± 0.0226	18.90 ± 0.000	-93.50 ± 0.849	90	8.2107211e-3 +/- 5.3440405e-3
GLM-17	2020-03-03	12:33:27	0.062 ± 0.0007	18.25 ± 0.071	-106.35 ± 0.636	77	3.4441157e-3 +/- 2.4922397e-3
GLM-18	2020-03-31	19:31:52	0.105 ± 0.0573	28.45 ± 0.071	-112.05 ± 0.636	61	7.2469897e-3 +/- 4.7924800e-3
GLM-19	2020-04-08	16:25:28	0.120 ± 0.0926	26.10 ± 0.000	-93.90 ± 0.849	78	4.0292119e-3 +/- 2.8626279e-3
GLM-20	2020-04-18	17:43:25	0.139 ± 0.0106	29.00 ± 0.000	-106.55 ± 0.919	82	5.8303967e-3 +/- 3.9618242e-3
GLM-21	2020-04-20	16:05:22	0.318 ± 0.1655	28.15 ± 0.071	-97.85 ± 1.061	88	0.031378060 +/- 0.016913982
GLM-22	2020-04-25	11:03:09	0.323 ± 0.0813	32.15 ± 0.071	-111.60 ± 1.131	84	0.021997346 +/- 0.012507576
GLM-23	2020-04-28	19:31:52	0.105 ± 0.0573	28.45 ± 0.071	-112.05 ± 0.636	29	0.12687833 +/- 0.053736010
GLM-24	2020-05-08	10:06:16	0.490 ± 0.0750	21.60 ± 0.000	-92.40 ± 0.849	81	0.033207253 +/- 0.017743607
GLM-25	2020-07-15	19:58:28	0.693 ± 0.0495	24.00 ± 0.000	-108.35 ± 0.495	53	0.020548979 +/- 0.011800641
GLM-26	2020-08-07	13:29:57	0.163 ± 0.0057	28.80 ± 0.000	-106.05 ± 0.919	89	0.014606987 +/- 8.8040841e-3
GLM-27	2020-09-13	16:41:59	0.184 ± 0.0078	28.45 ± 0.071	-113.75 ± 0.919	85	0.010995616 +/- 6.8881646e-3
GLM-28	2020-09-30	12:28:11	0.100 ± 0.0078	24.90 ± 0.000	-110.90 ± 0.849	83	0.014013965 +/- 8.4951275e-3
GLM-29	2020-11-16	12:28:11	0.100 ± 0.0078	24.90 ± 0.000	-110.90 ± 0.849	106	0.052044572 +/- 0.025868548
GLM-30	2020-11-17	12:53:41	0.404 ± 0.0262	23.00 ± 0.000	-102.45 ± 0.919	93	0.060624247 +/- 0.029367156
GLM-31	2020-12-19	10:18:14	0.407 ± 0.0110	21.95 ± 0.071	-101.60 ± 0.990	98	0.060272985 +/- 0.029225978
GLM-32	2020-12-23	09:43:01	0.148 ± 0.0014	25.75 ± 0.071	-111.25 ± 0.778	81	0.012127937 +/- 7.4982028e-3
GLM-33	2020-12-29	15:20:54	0.118 ± 0.0014	16.80 ± 0.000	-102.20 ± 0.707	81	0.013161054 +/- 8.0470909e-3
GLM-34	2021-03-31	09:01:17	0.753 ± 0.3083	20.15 ± 0.071	-92.95 ± 0.212	24	0.054259119 +/- 0.026782008
GLM-Ven	2019-06-22	21:25:45	4.873 ± 0.0000	14.9 ± 0.000	-65.8 ± 0.000	25	6.1014359 +/- 0.81239700

Table 2. List of bolides detected in mexican territory (plus one detected near Venezuela and one detected near Cuba), detected by USG sensors.

ID	Date of event	Start Time (UT)	Velocity (km/s)				Latitude (deg)	Longitude (deg)	Altitude (km)	Energy (kT)
			v	v_x	v_y	v_z				
USG-01	1995-08-05	17:14:10					11.6	-104.3		0.56
USG-02	1996-07-12	14:04:45					20.7	-93.6		0.11
USG-03	1997-10-09	18:47:15					31.8	-106.0	37.0	0.53
USG-04	2000-01-18	08:33:58					24.3	-94.9		0.12
USG-05	2000-08-25	01:12:25					14.5	-106.1		3.1
USG-06	2005-11-15	05:19:07					26.3	-113.4	32.4	0.089
USG-07	2015-07-19	07:06:26	17.8	9.4	13.0	7.8	20.6	-87.6	22.0	0.082
USG-08	2019-02-01	18:17:10	16.3	-2.4	13.6	8.7	22.5	-83.8	23.7	1.4
USG-09	2019-06-22	21:25:48	14.9	-13.4	6.0	2.5	14.9	-66.2	25.0	6.0
USG-10	2020-04-28	05:43:17					20.1	-109.4		0.076

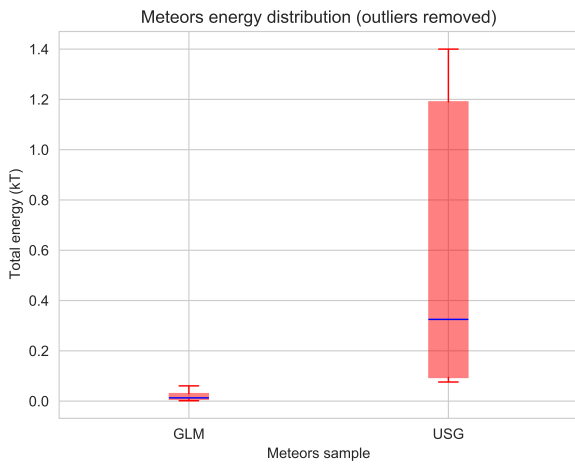

Fig. 2. Comparison between released energies of bolides detected by the Geostationary Lightning Mapper and USG sensors.

L_i of the frequency f_i (Emery & Camps, 2017):

$$L_i = s_i - \frac{40.3082\,\mathrm{m}^3\,\mathrm{s}^{-1}}{f_i^2} sTEC_i \tag{1}$$

Combining two observations at two different frequencies f_1 and f_2 we may obtain two different phase delays L_1 and L_2 and derive the TEC along the signal path:

$$sTEC = \frac{f_1^2 f_2^2 (L_1 - L_2)}{40.3082\,\mathrm{m}^3\,\mathrm{s}^{-1}\left(f_1^2 - f_2^2\right)} \tag{2}$$

In the other hand, the Vertical Total Electron Content (vTEC) is computed from the sTEC as follows (Kumar et al., 2012):

$$vTEC = \frac{sTEC - [b_R + b_S]}{S(\theta_I)} \tag{3}$$

where b_R and b_S are receiver and satellite biases, respectively. θ_I is the elevation angle in degrees, $S(\theta_I)$ is the obliquity factor with zenith angle ψ at the Ionospheric Pierce Point (IPP):

$$S(\theta_i) = \frac{1}{\cos\psi} = \left\{1 - \frac{R_E \cos\theta_I}{R_E + h}\right\}^{-1/2} \tag{4}$$

Where R_E is the Earth radius in km and $h = 350\,\mathrm{km}$ is the ionospheric shell above the earth's surface.

Both parameters sTEC and vTEC are computed using a software developed by Gopi K. Seemala, publicly available at `https://seemala.blogspot.com/`.

3. Bolides physical parameters

Enter Raul's work here

4. Ionospheric background and vTEC maps

In progress ...

5. Discussion

Enter discussion here

6. Acknowledgments

The RINEX data used in this paper were obtained from the Trans-boundary, Land and Atmosphere Long-term Observational and Collaborative Network (TLALOCNet, Cabral-Cano et al. (2018)), operated by the Servicio de Geodesia Satelital (SGS) at the Instituto de Geofísica-Universidad Nacional Autónoma de México (UNAM) in collaboration with UNAVCO Inc.

We are deeply grateful to all personnel from SGS, SSN and UNAVCO for station installation, maintenance, data acquisition, IT support and data curation and distribution for these networks and in particular to the following individuals and institutions, and those whose hard field work and resourcefulness were central to the success of this project: Bill Douglass, Neal Lord and Bill Unger at UW-Madison, Oscar Diaz-Molina and Luis Salazar-Tlaczani at SGS, John Galetzka, Adam Wallace, Shawn Lawrence, Sean Malloy and Chris Walls at UNAVCO, Jesus Pacheco-Martínez at Universidad Autónoma de Aguascalientes, Bertha Marquez-Azúa and personnel at the Universidad de Guadalajara at campus Guadalajara, Mascota and Ameca, Protección Civil de Jalisco, Universidad de Colima at campus Colima and campus El Naranjo and Centro de Geociencias, Centro de Ciencias de la Atmosfera Instituto de Biología Estacion Chamela at UNAM. TLALOCNet, SSN-TLALOCNet and other GPS related operations from SGS are supported by CONACyT projects 253760, 256012 and 2017-01-5955, UNAM-PAPIIT projects IN104213, IN111509, IN109315-3, IN104818-3, NSF grant 2025104, NASA-ROSES grant NNX12AQ08G and supplemental support from UNAM-Instituto de Geofísica. UNAVCO's initial support for TLALOCNet (some of its stations now part of the GAGE Facility-NOTA) was performed under EAR-1338091 and is currently supported by NSF and NASA under NSF Cooperative Agreement EAR-1724794.

Also we are grateful with the Dirección General de Asuntos Académicos (DGAPA) of the Universidad Nacional Autónoma de México and the Programa de Becas Posdoctorales for funding this project.

Appendix A. Estimation of distances to meteors

The distance between the GOES satellite and the meteor, neccesary to estimate the radiated energy is calculated as follows:

$$R = \left|\vec{r}_{GLM} - \vec{r}_{obj}\right| \tag{A.1}$$

where $\vec{r}_{GLM}$ is the vector position of the GLM satellite and $\vec{r}_{obj}$ is the vector position of the meteor.

In cartesian coordinates, the distance R is given by:

$$R = \Big((x_{GLM} - x_{obj})^2 + (y_{GLM} - y_{obj})^2 + (z_{GLM} - z_{obj})^2\Big)^{1/2} \tag{A.2}$$

$$\tag{A.3}$$

The transformation to spherical coordinates is given by:

$$x = r\cos\phi\cos\theta \tag{A.4}$$

$$y = r\sin\phi\cos\theta \tag{A.5}$$

$$z = r\sin\theta \tag{A.6}$$

Where r is measured from the center of the earth, $-180^\circ <$ phi $<= 180^\circ$ represents the longitude; is positive at east of Greenwich meridian, and negative eastwards. $90^\circ <= \theta <= 90^\circ$ represents the latitude and is positive at the north of equator and negative southwards.

Substituting the transform (A.4 - A.6) into (A.2), using elemental trigonometry and considering both GLM satellites lie into the equator ($\theta_{GLM} = 0$) we get:

$$R^2 = r_{GLM}^2 + r_{obj}^2 - 2r_{GLM}r_{obj}f(\theta_{obj}, \phi_{obj}, \phi_{GLM}) \tag{A.7}$$

$$\text{where}: f(\theta_{obj}, \phi_{obj}, \phi_{GLM}) = \cos\theta_{obj}\cos\Big(\phi_{GLM} - \phi_{obj}\Big) \tag{A.8}$$

Since r_{GLM} and r_{obj} are measured from the center of the arth ge find that:

$$r_{GLM} = r_{earth} + h_{GLM} \tag{A.9}$$

$$r_{obj} = r_{earth} + h_{obj} \tag{A.10}$$

Substituting (A.9, A.10) into A.7 and considering that $h_{obj} \ll h_{GLM}$ we get:

$$R^2 = 2r_{earth}^2\Big(1 - f(\theta_{obj}, \phi_{obj}, \phi_{GLM})\Big) + 2r_{earth}h_{GLM}$$
$$\Big(1 - f(\theta_{obj}, \phi_{obj}, \phi_{GLM})\Big) + h_{GLM}^2 - 2h_{GLM}h_{obj}f(\theta_{obj}, \phi_{obj}, \phi_{GLM}) \tag{A.11}$$

Appendix B. Energy estimation

The total radiant energy emmited is calculated integrating over all the time and all directions. The first is obtained simply summing all the light curve points. In the other hand, to integrate over all directions, we multiply the GLM event energies by the factor $(1.695 \times 10^{18})(1.018 \times 10^3)\Big(\frac{R}{35780\ km}\Big)^2$ (Jenniskens et al., 2018). This factor also considers that the GLM only detects light from the OI line. Then, we obtain the luminous efficiency τ_1 (i.e the fraction of the total energy converted into radiation) following Brown et al. (2002):

$$\tau_1 = (0.1212 \pm 0.0043)E_0^{0.115\pm0.075} \tag{B.1}$$

Where E_0 is the luminous energy calculated from integrating GLM reported energies (in kilotons). Finally the total estimated

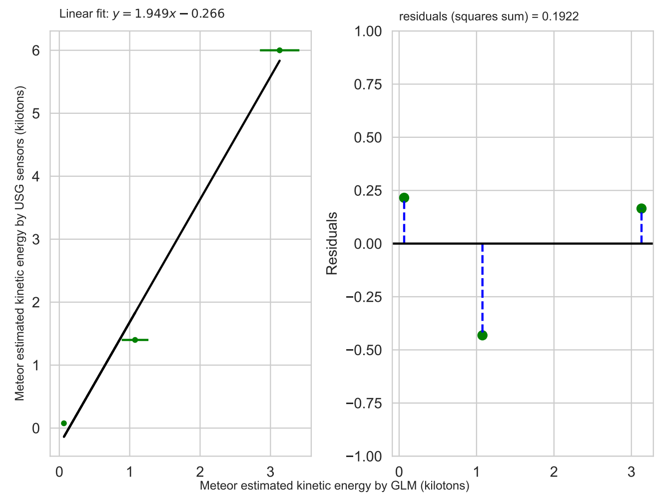

Fig. B.3. Left: Linear fit between energies calculated from GLM data and energies reported by USG sensors. Right: Residuals of the fit, used as error in the recallibration factor. The three events used for this linear fit are GLM-00 (the cuban meteoroid), GLM-23 and GLM-Ven (Venezolan meteoroid).

energy is $E = E_0/\tau_1$. We may compare the resulting GLM energies with the energies reported by USG sensors using the events which belong to both samples, and we noticed that the energies obtained with GLM data is systematically lower than the energies reported by the USG sensors. In this work we assumed that this discrepancy is due to the GLM sensors does not detect the full meteor paths, just a fraction of the total radiated energy. To solve this problem we made a linear fit between the derived energies and the energies reported in the USG sample for the events which appear in both samples, and recallibrate the energies of the rest of the GLM sample. The linear fit is shown in figure B.3. We used the linear fit slope as the recallibration factor and the residuals as the error, we neglected the y-intercept term because this term is much larger than the most energies in the GLM sample and strongly affects the recallibrated energy.

References

Blanco-Cano, X., Omidi, N., & Russel, C. T. (2004). How to make a magnetosphere. *Astronomy & Geophysics*, *45*(3), 3.14–3.17. doi:10.1046/j.1468-4004.2003.45314.x.

Brown, P., Spalding, R. E., ReVelle, D. O., Tagliaferri, E., & Worden, S. P. (2002). The flux of small near-Earth objects colliding with the Earth. Nature, *420*(6913), 294–296. doi:10.1038/nature01238.

Cabral-Cano, E., Pérez-Campos, X., Márquez-Azúa, B., Sergeeva, M. A., Salazar-Tlaczani, L., DeMets, C., Adams, D., Galetzka, J., Hodgkinson, K., Feaux, K., Serra, Y. L., Mattioli, G. S., & Miller, M. (2018). TLALOCNet: A Continuous GPS-Met Backbone in Mexico for Seismotectonic and Atmospheric Research. *Seismological Research Letters*, *89*(2A), 373–381. doi:10.1785/0220170190.

Chilcote, M., LaBelle, J., Lind, F. D., Coster, A. J., Miller, E. S., Galkin, I. A., & Weatherwax, A. T. (2015). Detection of traveling ionospheric disturbances by medium-frequency doppler sounding using am radio transmissions. *Radio Science*, *50*(3), 249–263. doi:https://doi.org/10.1002/2014RS005617.

Cnossen, I., Wiltberger, M., & Ouellette, J. E. (2012). The effects of seasonal and diurnal variations in the earth's magnetic dipole orientation on solar wind–magnetosphere-ionosphere coupling. *Journal of Geophysical Research: Space Physics*, *117*(A11). doi:https://doi.org/10.1029/2012JA017825.

Emery, W., & Camps, A. (2017). Chapter 6 - remote sensing using global navigation satellite system signals of opportunity. In W. Emery, & A. Camps (Eds.), *Introduction to Satellite Remote Sensing* (p. 455–564). Elsevier. doi:10.1016/B978-0-12-809254-5.00006-3.

Goodman, S. J., Blakeslee, R. J., Koshak, W. J., Mach, D., Bailey, J., Buechler, D., Carey, L., Schultz, C., Bateman, M., McCaul, E., & Stano, G. (2013). The goes-r geostationary lightning mapper (glm). *Atmospheric Research*, *125-126*, 34–49. doi:https://doi.org/10.1016/j.atmosres.2013.01.006.

Helmboldt, J. F., Lane, W. M., & Cotton, W. D. (2012). Climatology of midlatitude ionospheric disturbances from the very large array low-frequency sky survey. *Radio Science*, *47*(5). doi:https://doi.org/10.1029/2012RS005025.

Jenniskens, P., Albers, J., Tillier, C. E., Edgington, S. F., Longenbaugh, R. S., Goodman, S. J., Rudlosky, S. D., Hildebrand, A. R., Hanton, L., Ciceri, F., Nowell, R., Lyytinen, E., Hladiuk, D., Free, D., Moskovitz, N., Bright, L., Johnston, C. O., & Stern, E. (2018). Detection of meteoroid impacts by the geostationary lightning mapper on the goes-16 satellite. *Meteoritics & Planetary Science*, *53*(12), 2445–2469. doi:https://doi.org/10.1111/maps.13137.

Kumar, D. S., Priyadarshi, S., Seemala, G., & Singh, A. (2012). Gps-tec variations during low solar activity period (2007-2009) at indian low latitude stations. *Astrophysics and Space Science*, *339*, 165–178. doi:10.1007/s10509-011-0973-6.

Lin, C. H., Lin, J. T., Chen, C. H., Liu, J. Y., Sun, Y. Y., Kakinami, Y., Matsumura, M., Chen, W. H., Liu, H., & Rau, R. J. (2014). Ionospheric shock waves triggered by rockets. *Annales Geophysicae*, *32*(9), 1145–1152. doi:10.5194/angeo-32-1145-2014.

Oka, M., Phan, T.-D., Eastwood, J. P., Angelopoulos, V., Murphy, N. A., Øieroset, M., Miyashita, Y., Fujimoto, M., McFadden, J., & Larson, D. (2011). Magnetic reconnection x-line retreat associated with dipolarization of the earth's magnetosphere. *Geophysical Research Letters*, *38*(20). doi:https://doi.org/10.1029/2011GL049350.

Rodríguez-Martínez, M., Pérez-Enríquez, H. R., Carrillo-Vargas, A., López-Montes, R., Araujo-Pradere, E. A., Casillas-Pérez, G. A., & Cruz-Abeyro, J. A. L. (2014). Ionospheric disturbances and their impact on ips using mexart observations. Sol Phys, *289*, 2677–2695. doi:https://doi.org/10.1007/s11207-014-0496-8.

Rumpf, C. M., Longenbaugh, R. S., Henze, C. E., Chavez, J. C., & Mathias, D. L. (2019). An algorithmic approach for detecting bolides with the geostationary lightning mapper. *Sensors*, *19*(5). URL: https://www.mdpi.com/1424-8220/19/5/1008. doi:10.3390/s19051008.

Sergeeva, M. A., Demyanov, V. V., Maltseva, O. A., Mokhnatkin, A., Rodriguez-Martinez, M., Gutierrez, R., Vesnin, A. M., Gatica-Acevedo, V. J., Gonzalez-Esparza, J. A., Fedorov, M. E., Ishina, T. V., Pazos, M., Gonzalez, L. X., Corona-Romero, P., Mejia-Ambriz, J. C., Gonzalez-Aviles, J. J., Aguilar-Rodriguez, E., Cabral-Cano, E., Mendoza, B., Romero-Hernandez, E., Caraballo, R., & Orrala-Legorreta, I. D. (2021). Assessment of morelian meteoroid impact on mexican environment. *Atmosphere*, *12*(2). doi:10.3390/atmos12020185.

Vázquez, M., Vaquero, J. M., Gallego, M. C., Roca Cortés, T., & Pallé, P. L. (2016). Long-Term Trends and Gleissberg Cycles in Aurora Borealis Records (1600 - 2015). Sol Phys, *291*(2), 613–642. doi:10.1007/s11207-016-0849-6.

Vlasov, M. N., & Kelley, M. C. (2010). Crucial discrepancy in the balance between extreme ultraviolet solar radiation and ion densities given by the international reference ionosphere model. *Journal of Geophysical Research: Space Physics*, *115*(A8). doi:https://doi.org/10.1029/2009JA015103.

Yang, Y.-M., Komjathy, A., Langley, R. B., Vergados, P., Butala, M. D., & Mannucci, A. J. (2014). The 2013 chelyabinsk meteor ionospheric impact studied using gps measurements. *Radio Science*, *49*(5), 341–350. doi:https://doi.org/10.1002/2013RS005344.

Zolesi, B., & Cander, L. R. (2014). *Ionospheric Prediction and Forecasting*.